Click Here for Full Article

Diagnostic analyses of a regional air quality model: Changes in modeled processes affecting ozone and chemical-transport indicators from NO_x point source emission reductions

J. M. Godowitch,[1] C. Hogrefe,[2] and S. T. Rao[1]

[1]   The impact of nitrogen oxide (NO_x) emission reductions from major point sources on the key physical and chemical processes contributing to ozone formation and accumulation is studied, and the extent of change in the chemical regime is examined using selected photochemical indicators in the eastern United States. The Community Multiscale Air Quality (CMAQ) chemical-transport model, equipped with the process analysis technique, was applied in modeling scenarios involving 2002 base case emissions and an emissions scenario containing real-world point source NO_x reductions implemented before the summer ozone season of 2004. Spatial patterns and temporal variations in process rates and changes in chemical-transport indicators are highlighted from results of summer 2002 days, representative of generally southwesterly wind flows across the Midwestern source region with ozone transport toward the northeastern states. Substantial decreases exceeding 50% in O_3 chemical production rates were associated with the largest NO_x point source emission reductions, causing declines in ozone concentrations at the surface and aloft in downwind areas. The decreases in the various physical processes and their spatial difference patterns closely resembled the change in maximum O_3 concentrations. The net ozone production efficiency was found to increase, since the decline in O_3 concentrations was less than the decrease in reactive nitrogen products (NO_z). The O_3/NO_x ratio also increased between the base case and NO_x reduction scenario results, indicating a noticeable shift in the chemical regime toward more NO_x-limited conditions in plume-impacted areas downwind of the sources. The drop in surface NO_x concentrations in modeled and observed results at a location just downwind of the Ohio River Valley source region is attributable to the point source NO_x emission reductions.

1.   Introduction

[2]   The formation and accumulation of tropospheric ozone are dependent upon atmospheric physical and chemical processes. The key physical processes, acting on existing ozone, involve meteorological mechanisms including transport and diffusion in the horizontal and vertical dimensions, and pollutant removal through dry and wet deposition. Since O_3 is primarily a secondary species, formation of new ozone largely occurs through complex interactions of numerous atmospheric photochemical reactions involving a variety of volatile organic compounds (VOC) and nitrogen oxide ($NO_x = NO + NO_2$) that are emitted from various anthropogenic and natural sources. Consequently, a substantial change in the emission rates of these key precursor species is expected to strongly influence ozone chemical production, and subsequently the ozone concentration levels across a region.

[3]   Results of both modeling studies [*Frost et al.*, 2006; *Kim et al.*, 2006; *Godowitch et al.*, 2008; *Gilliland et al.*, 2008] and observation-based analyses [*Environmental Protection Agency*, 2005; *Gego et al.*, 2007] have demonstrated decreases in maximum ozone concentrations in the eastern United States. The significant NO_x emission reductions from major point sources, primarily power plants, which were implemented by the U.S. Environmental Protection Agency's (EPA) NO_x SIP (State Implementation Plan) Call control program, are partially attributed for the noticeable improvement in ozone air quality between 2002 and 2004 [*Environmental Protection Agency*, 2005]. *Kim et al.* [2006] showed comparable decreases of NO_2 in vertical columns from both satellite-based measurement results and

---

[1]Atmospheric Sciences Modeling Division, Air Resources Laboratory, National Oceanic and Atmospheric Administration, Research Triangle Park, North Carolina, USA.
[2]Atmospheric Sciences Research Center, University at Albany, State University of New York, Albany, New York, USA.

vertically integrated modeled NO$_2$ concentrations, which correlated well with NO$_x$ emission reductions, particularly over the greater Ohio River Valley source region. Their model simulations also exhibited decreases in O$_3$ concentrations between the base emissions case and reduced NO$_x$ emission scenarios under summer 2004 conditions. Using a dynamic model evaluation approach, which entails assessing a model's ability to reproduce observed concentration changes due to changes in total emissions and meteorology, *Gilliland et al.* [2008] reported general agreement between modeled and observed results in showing notable decreases in daily maximum 8-h O$_3$ concentrations at sites across the eastern U.S. between 2002 and 2004. Although the observational results displayed somewhat greater ozone response than those generated from the model, results varied among the chemical mechanisms. Nevertheless, this evidence from observations and models of O$_3$ concentration change signifies that effects on the relevant processes governing O$_3$ formation and accumulation have concurrently occurred.

[4] In this paper, diagnostic analysis tools are applied to provide insights into the impacts from recent changes in NO$_x$ point source emissions alone on the relevant process rates governing O$_3$ concentrations and on the chemical regime. In particular, the spatial variability and temporal behavior of the individual process rates are examined by focusing on changes in the process rates within plume-impacted areas downwind of major point sources. The diagnostic analyses are performed on modeling results of base case and emission reduction scenarios from photochemical simulations with the Community Multiscale Air Quality (CMAQ) model using process analysis (PA), an innovative diagnostic technique. Other modeling efforts have also taken advantage of PA to investigate the relative contributions of the physical and chemical processes on O$_3$ concentrations at select urban and nonurban grid cells with different model grid resolutions [*Jang et al.*, 1995], to assess differences in process rates between two different photochemical models [*O'Neill and Lamb*, 2005], and to study the magnitudes of key processes, particularly O$_3$ chemical production differences between two days in selected grid cells containing ozone measurement sites and in a Lagrangian mode along a back trajectory [*Jiang et al.*, 2003]. Process analysis results in these modeling studies provided valuable quantitative information at selected grid cells about the relative contributions of the individual process rates to O$_3$ concentrations. During our model runs, the PA technique also provided a complete suite of hourly individual process rate values. Additionally, our analysis effort involves plume-impacted areas downwind of numerous major point sources as well as the entire modeling domain of the eastern United States in an effort to derive a regional perspective of the magnitudes of key process rates, and their spatial and temporal changes due to point source NO$_x$ emission differences between a base case and emission reduction modeling scenarios.

[5] Although the CMAQ modeling period spanned a 3-month period during summer 2002, the results reported herein were obtained from model simulations for set of selected case study days exhibiting fair weather conditions with a southwestern flow pattern across the Ohio River Valley. The magnitudes and change in O$_3$ chemical production rate are emphasized owing to the critical role of the

photochemistry process in ozone formation under these favorable conditions. Although various species indicator ratios are proposed for identifying NO$_x$ and VOC sensitive conditions [*Sillman*, 1999], our analysis examines the O$_3$/NO$_x$ ratio and the O$_3$ to NO$_z$ relationship in order to give insight about the effects on the chemical state across the region from the NO$_x$ point source emission reductions. Additionally, the spatial correlation of O$_3$ in terms of a spatial scale (defined by the e-folding distance) induced by the synoptic-scale forcing is also examined to explore the change due to both emissions and meteorological differences from a set of modeling scenarios.

2. Model Description, Input Data, and Modeling Scenarios

[6] The Community Multiscale Air Quality (CMAQ) model, a comprehensive Eulerian air quality grid model, was applied in this modeling effort. The CMAQ model is designed for use in assessments of multiple atmospheric pollutants, including O$_3$ and other oxidants, aerosols, selected air toxic and mercury species on temporal and spatial scales from urban to continental domains. The CMAQ model contains state-of-science algorithms to simulate the relevant physical, chemical, and atmospheric removal processes governing a broad array of species concentrations. In particular, the model was configured to treat horizontal and vertical advection, turbulent diffusion in the horizontal and vertical based on K-theory, gaseous and aqueous phase chemistry, cloud effects on photolysis rates, pollutant dry deposition, and wet removal processes. For the photochemical simulations performed in this study, the Carbon Bond IV (CB4) gas-phase chemical mechanism was applied. The CB4 chemical mechanism included updates described by *Byun and Schere* [2006]. The theoretical formulations and numerical algorithms employed to solve the physical and chemical processes incorporated into the CMAQ model are described in greater detail by *Byun and Schere* [2006].

[7] The process analysis (PA) technique is a valuable mass balance method contained in the CMAQ model code. The PA approach was exercised during this modeling effort in order to generate quantitative information about the relative contributions from the individual process terms contained in the mass conservation equations being solved for each pollutant species. With the operator-splitting approach employed in CMAQ, the partial differential equations are solved separately for each process in a sequential manner at 12 min model time steps, and the contributions of each process affecting the change in the species concentration are integrated over 1-h intervals. Thus, the PA results generated for the 3-D array of grid cells represent integrated process rates (IPR). During a model simulation, IPR values (units; ppb/h) for the following physical and chemical processes were computed and archived at the end of each hour at the same time as the species concentrations: horizontal advection (ΔC_{hadv}), vertical advection (ΔC_{vadv}), horizontal diffusion (ΔC_{hdif}), vertical mixing (ΔC_{vdif}), dry deposition (ΔC_{ddep}), net chemical production/loss (ΔC_{chem}), aqueous (cloud) chemistry (ΔC_{clds}), and emissions (ΔC_{emis}). There is no ΔC_{emis} term for O$_3$. The net change in species concentration over an hour interval can be obtained from the sum of these IPR terms. Although
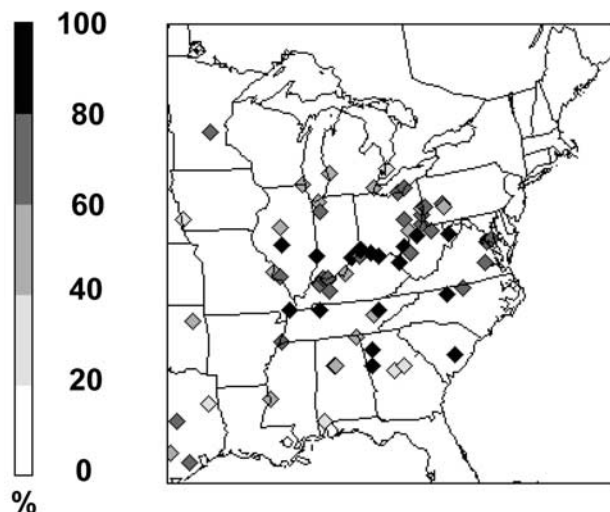
Figure 1. Reduction (%) in NO$_x$ emissions at major point sources in the modeling domain between the M02E02 and M02E04 scenarios from a case study day (11 August 2002).

considerable flexibility exists with the PA technique built into the CMAQ for the specification of species and grid cells of interest [*Gipson*, 1999], the PA method was configured to generate IPR values for O$_3$, as well as other species, over the entire modeling domain.

[8] The 2-D and 3-D meteorological fields for the CMAQ model simulations were generated by the Penn State/NCAR fifth-generation mesoscale model (MM5) [*Grell et al.*, 1994]. The MM5 model (version 3.6.3) was applied in a nonhydrostatic mode and for these retrospective periods the four-dimensional data assimilation (FDDA) technique was also applied to take advantage of available observed wind, temperature, and moisture data to provide more accurate model fields. An improved land-surface scheme [*Xiu and Pleim*, 2001] was also applied to improve model response to varying soil moisture and vegetation conditions over the summer season. The CMAQ Meteorology-Chemistry Interface Processor (MCIP v3.1) program was exercised to extract and reformat the MM5 output from 30 levels and prepared data sets containing the hourly meteorological parameter fields for the 14 vertical layers utilized in the CMAQ simulations.

[9] The 3-D emission data sets for this chemical mechanism were obtained by applying the comprehensive Sparse Matrix Operator Kernel Emissions (SMOKE) processing system (http://www.smoke-model.org). The EPA National Emissions Inventory (NEI) 2001 (http://www.epa.gov/ttn/chief/net/critsummary.html) anthropogenic emissions were updated to generate surface and elevated non-CEMS point source emissions. Biogenic emissions of NO$_x$, isoprene, and other naturally emitted VOC species were computed by the Biogenic Emissions Inventory System model (BEIS version 3.13). The MOBILE6 model was applied by utilizing projections of vehicle-miles-traveled (VMT) and fleet factors to develop gridded motor vehicle emissions for the summer 2002 and 2004 periods [*Gilliland et al.*, 2008].

[10] The key NO$_x$ emission category for this study is the major point source sector, which primarily includes electri-

cal generating units (EGUs) at fossil-fuel power plants and large industrial sources. These point sources are equipped with Continuous Emission Monitoring Systems (CEMS) in order to provide direct measurements of NO$_x$ and SO$_2$ emissions. The hourly CEMS data from the summer periods of 2002 and 2004 were incorporated into the layers containing the plume heights within the 3-D emissions files in this modeling effort, rather than deriving hourly emissions from temporal profiles based on the annual point source emission inventory.

[11] The locations of major CEMS point sources in the modeling domain along with the percentage change in their NO$_x$ emissions stemming from the NO$_x$ SIP Call program are displayed in Figure 1. These high NO$_x$ point sources are located away from urban emission areas in relatively undeveloped areas. NO$_x$ emission reductions of up to 90% occurred at numerous individual sources, particularly at the largest NO$_x$-emitting point sources found within the Ohio River Valley (ORV) region. Large NO$_x$ emission reductions are also apparent at point sources found outside the ORV. However, most of these sources are relatively isolated and not in as close proximity to each other as those situated in the ORV region. Key characteristics about these continuous emissions from point sources are their elevated release (stack heights ≈100–300 m AGL) and their plumes also exhibit additional rise due to buoyancy. In fact, the largest amounts of these NO$_x$ point source emissions were found in model layers at heights of about 400–600 m [*Godowitch et al.*, 2008, Figure 3]. Horizontal transport of NO$_x$ concentrations at these altitudes is more pronounced compared to near-surface releases owing to higher winds aloft, particularly during the nocturnal period.

[12] The CMAQ modeling domain encompassed the eastern half of the United States and southeastern Canada with 205 × 199 horizontal grid cells exhibiting a 12-km grid resolution. The vertical structure consisted of 14 layers extending from the surface (layer 1 thickness is near 40 m) to over 15 km on a sigma-pressure, terrain-following coordinate system. The initial conditions and lateral boundary concentrations for each modeling scenario were prescribed by the same set of time-invariant, vertically varying tropospheric background values [*Byun and Ching*, 1999]. The model simulation periods were from 1 June through 31 August during 2002 and 2004. A 4-day simulation period served as a model spin-up period.

[13] A set of modeling scenarios was specifically designed to permit an investigation of the separate impacts on O$_3$ concentrations from changes in emissions and meteorology [*Godowitch et al.*, 2008]. However, the emission reductions at major NO$_x$ point sources with CEMS measurements are responsible for driving the differences in the key modeling scenarios examined herein. A base case emission scenario is designated as M02E02 and the NO$_x$ emission reduction scenario is defined as M02E04. These modeling results permit an assessment of the effect of point source emission changes on O$_3$ levels and individual process rates since the same summer 2002 meteorological conditions were applied in both modeling scenarios. Emissions by other NO$_x$ source sectors remained unchanged. Modeling scenarios for the summer 2004 period are designated as M04E04 (i.e., meteorology and emissions for 2004), while the M04E02 scenario involved 2002 CEMS
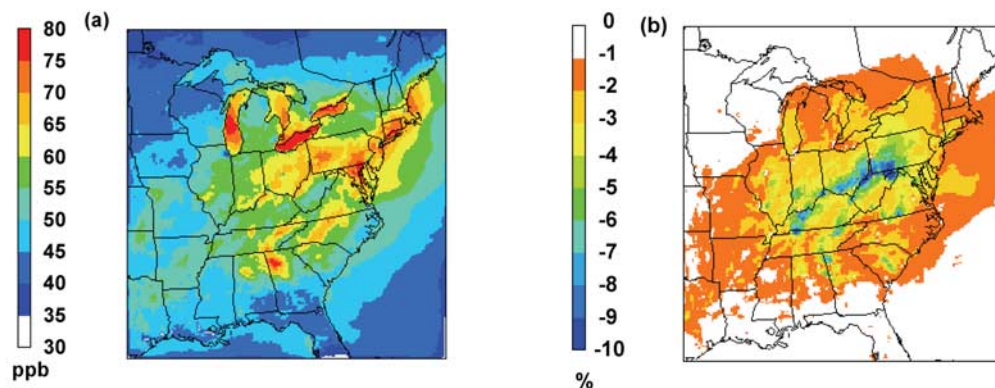
Figure 2. (a) Spatial field of the average daily maximum 8-h O$_3$ concentration from the M02E02 results and (b) average decrease (%) in daily maximum 8-h O$_3$ between the M02E02 and M02E04 scenarios for the summer case study days.

emissions. Two noteworthy hypothetical modeling scenarios exercised with 2002 summer meteorology involved; a simulation using biogenic emissions only with anthropogenic emissions zeroed out (M02ENA), and a simulation and results described by *Gego et al.* [2008], which assumed no point source emission control program with 1997 point source NO$_x$ emissions from the utility sector adjusted upward to 2002 demand levels (M02ENC).

3. Results and Discussion

[14] Although the modeling periods spanned 3-month summer periods exhibiting a variety of weather conditions and flow regimes, results from a group of summer 2002 days, displaying a prevailing southwesterly (SW) wind flow pattern across the ORV, were selected for analysis since the focus of this study is on examining regional transport of ozone and its precursors. The weather conditions across the eastern U.S. during the summer of 2002 were generally warmer and drier than those in the summer of 2004, which exhibited much cooler than normal temperatures and wetter conditions, and the region experienced few high-ozone events [*White et al.*, 2007]. The model results from the following set of days (4, 5, 11, 23, 26 June; 8, 22, 28 July; 11, 14, and 22 August 2002) were subjected to various diagnostic analysis methods. The meteorological pattern exemplified during these cases is a relatively common summer synoptic flow regime that is conducive to the occurrence of high ambient O$_3$ concentrations, namely a high-pressure system situated in the southeastern U.S. with the predominant transport from the Midwest into the northeastern states [*Hidy*, 2000]. By judicious selection of cases demonstrating a very similar flow pattern, common features in the spatial pattern and the temporal evolution for ozone and its process rates should emerge and the averaged results can be more easily interpreted. Hence, results from this subset of summer days, while representative of high O$_3$ days associated with this particular flow regime, are not representative of an entire summer season.

[15] The modeled daily maximum 8-h ozone concentrations from this set of case study days were among the highest over the entire summer period. The maximum 8-h O$_3$ concentration field shown in Figure 2a was determined by

averaging the results from all case study days. Relatively high ozone levels are found in various parts of the region including; the ORV region and extending into Pennsylvania, along the northeastern corridor of urban areas from Washington, DC through Boston, areas of the southeastern states and over the Great Lakes. Of particular interest, Figure 2b depicts the corresponding average percentage decrease in daily maximum 8-h O$_3$ between the results from the M02E02 and M02E04 scenarios across the region. A rather elongated area with a more pronounced decrease of modeled maximum ozone concentrations exists within the ORV region and downwind of it under this flow regime compared to results for other synoptic flow patterns during summer 2002 [*Godowitch et al.*, 2008]. The results in Figure 2b are attributed to the alignment of the numerous major point sources along the ORV region with the orientation of the prevailing wind flow pattern, which is believed to have accentuated the impact in the downwind area due to the large NO$_x$ emission reductions. The largest decreases in maximum 8-h ozone concentration of about 10% are found close to the ORV region. Other notable decreases in maximum ozone values are also associated with major point sources scattered throughout the region in Figure 1. In addition, the ozone reductions in Figure 2b are discernable in most of the region. It is also apparent that the differences in maximum 8-h O$_3$ between these scenarios diminished with increasing distance from the various source locations.

3.1. Spatial Variations in Process Rates and Their Change in the Modeling Domain

[16] The spatial pattern of the average O$_3$ chemical production rate over the region from M02E02 results during the time of maximum values and the companion spatial field of the difference in ΔC_{chem} between M02E02 and M02E04 results are displayed in Figures 3a and 3b, respectively. Significant spatial variability in O$_3$ chemical production exists across the domain in Figure 3a. In particular, high O$_3$ chemical production rates are evident downwind of the larger metropolitan urban areas, in close proximity of major NO$_x$ point source locations as well as over portions of the Great Lakes. High O$_3$ chemical production rates are certainly found in the ORV where numerous NO$_x$ point sources are situated. Large negative ΔC_{chem} values (i.e., ~ −20 to
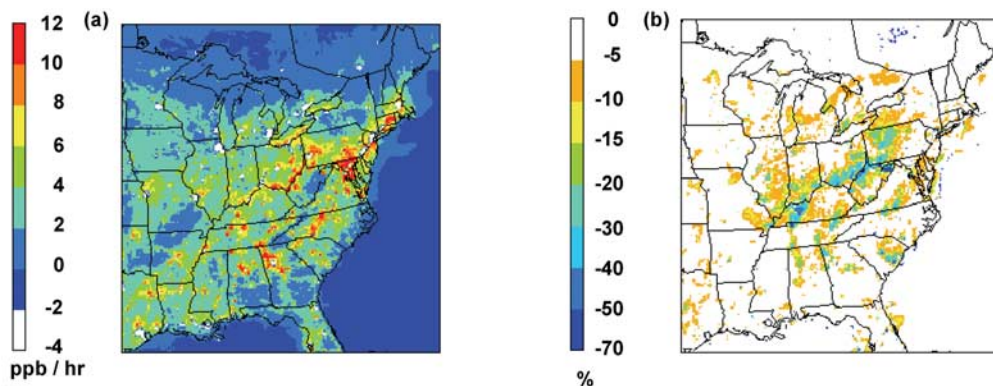
Figure 3. Spatial variation over the modeling domain at a midday hour (1630 UTC) of the (a) average O$_3$ chemical production rate (ΔC_{chem}) from the M02E02 scenario and (b) its percentage decrease [(M02E04 − M02E02) × 100/M02E02]. These results represent the average over all case study days.

−40 ppb/h) are evident in highly urbanized grid cells of the largest metropolitan areas owing to the high NO concentrations associated with mobile source emissions which cause considerable O$_3$ titration. It is noteworthy that areas exhibiting decreases of 20–30% in O$_3$ chemical production rates between the base case and emission reduction scenarios in Figure 3b occur within the ORV source region as well as the downwind area of western Pennsylvania. Notable decreases in ΔC_{chem} are also evident downwind of major point sources which experienced significant NO$_x$ emission reductions. The largest differences in ΔC_{chem} of up to 70% existing in the vicinity of point source locations are the subject of further analysis in a later section.

[17] The spatial field of average ΔC_{ddep} from the M02E02 scenario results is depicted in Figure 4a from a midafternoon hour when O$_3$ dry deposition remains active. The dry deposition process is modeled with the deposition velocity approach and the product of deposition velocity and concentration determines the pollutant deposition flux. Figure 4a reveals that larger O$_3$ dry deposition rates approaching −50 ppb/h occur in the same areas exhibiting the highest maximum O$_3$ concentrations. Furthermore, deposition velocities are derived from a series of resistances which depend on meteorological parameters and vary with

land-use type. Negligible O$_3$ deposition, as anticipated, occurs over water bodies owing to high surface resistance and relatively low dry deposition is also apparent in urban grid cells where the fractional area of vegetative land cover is rather small. Since the same deposition velocity fields were employed in both modeling scenarios, a change in deposition flux rates must be related to the changes in O$_3$ concentrations. Hence, the spatial pattern and the magnitude of the decrease in ΔC_{ddep} in Figure 4b closely resemble the results of the maximum O$_3$ concentration change in Figure 2b.

[18] Figure 5 displays the spatial pattern of ΔC_{vdif} for layer 1 from the M02E02 results and the spatial pattern of percentage change in ΔC_{vdif} between the M02E02 and M02E04 scenarios at the same time as the ΔC_{ddep} results. The largest vertical mixing rates for O$_3$ in Figure 5a reach nearly +50 ppb/h and are also found in the same areas as the highest O$_3$ concentrations illustrated in Figure 2a. Relatively large positive ΔC_{vdif} values are also distinguishable in major urban areas (e.g., Atlanta and Chicago) as higher O$_3$ from aloft is mixed downward to reinforce ozone being lost by chemical destruction noted earlier and to surface deposition loss. The decrease of ΔC_{vdif} between the results of these scenarios as shown in Figure 5b also displays the
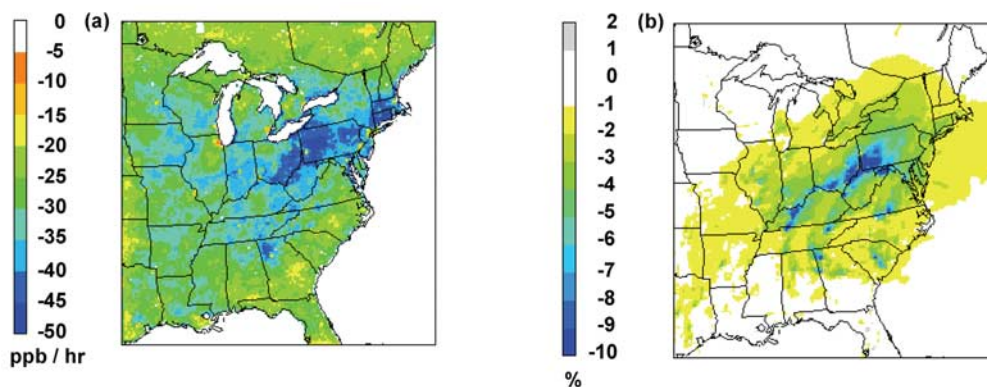

Figure 4. Spatial variation over the modeling domain at an afternoon hour (2030 UTC) of the (a) average dry deposition rate (ΔC_{ddep}) from the M02E02 scenario and (b) its percentage decrease [(M02E04 − M02E02) × 100/M02E02]. These results represent the average over all case study days.
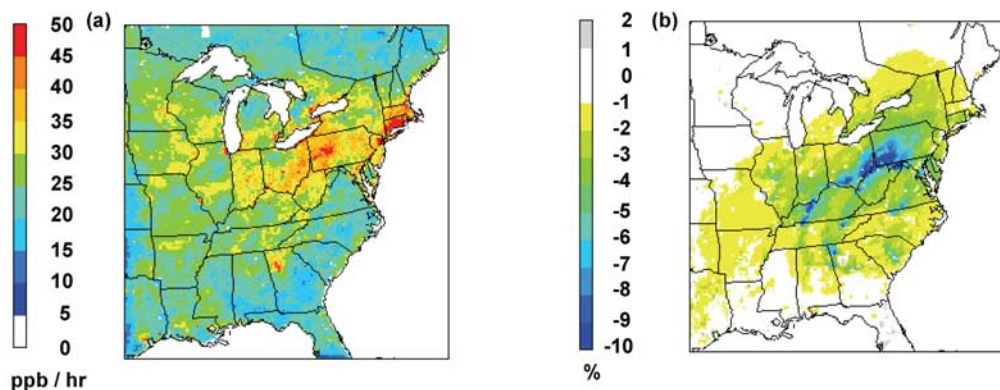
Figure 5. Spatial variation over the modeling domain at an afternoon hour (2030 UTC) of the (a) average vertical mixing term (ΔC_{vdif}) from the M02E02 scenario and (b) its percentage decrease [(M02E04 − M02E02) × 100/M02E02]. These results represent the average over all case study days.

same spatial pattern and percentage change as ΔC_{ddep} in Figure 4b.

[19] The spatial pattern of change in the horizontal advection process results (not shown) also closely mirrors the changes obtained in the physical processes described above. Since maximum O$_3$ concentrations declined from the M02E02 to M02E04 results, horizontal O$_3$ gradients were reduced. Thus, the horizontal advection rates, which are driven by spatial O$_3$ gradients, also declined in the M02E04 scenario.

3.2. Temporal Differences in Modeled Process Rates in Plume-Impacted Areas

[20] To investigate the evolution and differences in process rates over the course of the daytime period, this analysis focused on the areas impacted by change in the point source NO$_x$ emissions that emerged in the spatial patterns. Differences in total reactive nitrogen (NO$_y$ = NO$_x$ + nitric acid (HNO$_3$) + dinitrogen pentoxide (N$_2$O$_5$) + peroxyacetyl nitrate (PAN) + nitrous acid (HONO) + nitrate radical (NO$_3$) + peroxynitric acid (PNA)), derived from CB4 chemical mechanism species, provide a useful signature of hourly "plume prints" at the surface as a consequence of NO$_x$ emission reductions from individual major point sources. Plume-impacted areas in the domain emerge in Figure 6 from differences in ΔNO$_y$ (where ΔNO$_y$ = control NO$_y$ − base NO$_y$) during a typical afternoon hour due to differences in NO$_x$ emission rates between M02E02 and M02E04 scenarios. A negative ΔNO$_y$ value was utilized as a criterion in the same manner employed by *Frost et al.* [2006] to distinguish the grid areas impacted by point source plumes with emission reductions from those areas not influenced by the emission changes. NO$_y$ was adopted to identify the plume-print areas because of its longer lifetime than NO$_x$, which is more rapidly oxidized to reactive nitrogen products. The largest differences in NO$_y$ occurred in the source grid cells where the significant NO$_x$ emission reductions existed as denoted by the enlarged symbols displayed in Figure 6. Notable decreases in NO$_y$ are evident across the ORV region and downwind of it as ΔNO$_y$ tends to diminish away from the point source locations. A value of ΔNOy = −0.5 ppb was applied as a cutoff in specifying grid cells contained within a plume

print. Grid cells exhibiting more negative ΔNO$_y$ values than the cutoff value were included in subsequent analysis. By using ΔNO$_y$ as an indicator, specific plume-print grid patterns could also be linked to particular point sources for further analysis, especially in the case of more isolated sources.

[21] The temporal variation of the surface O$_3$ chemical production rate (ΔC_{chem}) from layer 1 during the daytime period is presented in Figure 7a. Hourly values, derived from all grids cells in plume prints for each case study day, and hourly average values over all days from the M02E02 and M02E04 scenarios reveal a strong variation in ΔC_{chem} over the daytime period. As expected, ΔC_{chem} exhibits a rapid rise during the morning period in correspondence with increasing photolysis rates. The highest O$_3$ production rates are reached near the midday hour (i.e., 1600–1700 UTC in this domain) and then a gradual decline in O$_3$ chemical
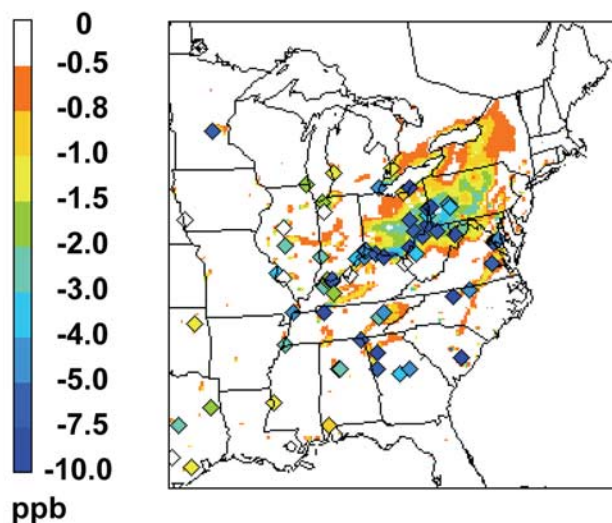

Figure 6. Spatial variation of the modeled NO$_y$ concentration difference between the NO$_x$ reduction and base case scenarios (M02E04 − M02E02) and at specific grid cells of major point sources (diamonds) at 1800 UTC on a case study day (11 August 2002).
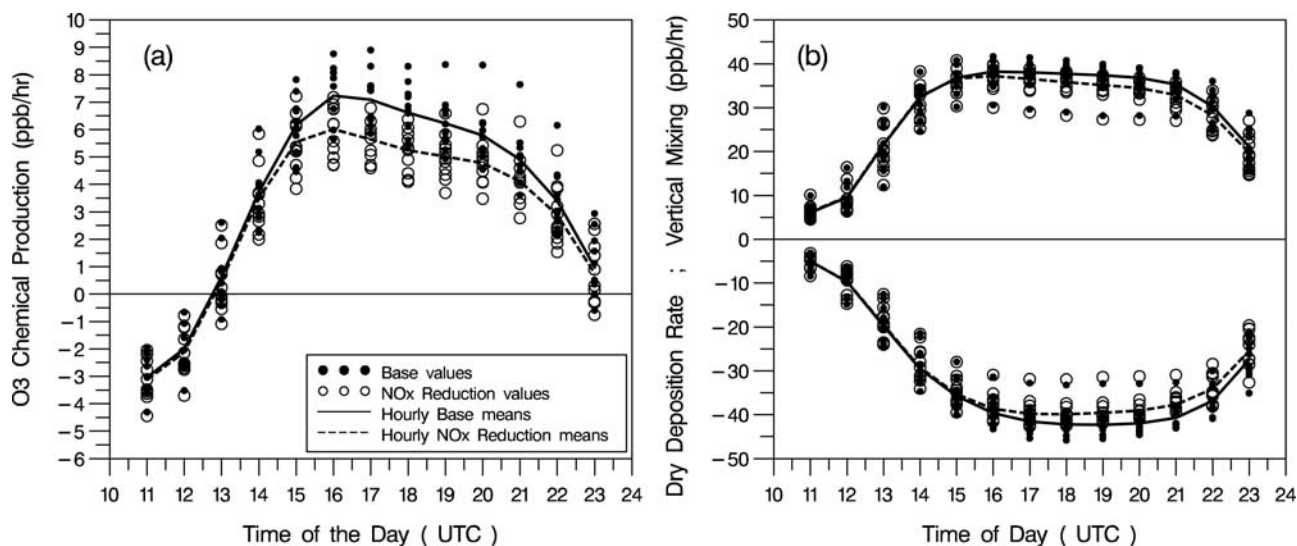
Figure 7. Temporal variation over the daytime period of the (a) O$_3$ chemical production rate (ΔC_{chem}) and (b) vertical mixing rate (ΔC_{vdif}) and dry deposition rate (ΔC_{ddep}) terms. Individual hourly values from the case study days in the M02E02 (solid circles) and M02E04 (open circles) scenario results were computed from grid cells in the plume-impacted zones (i.e., where $\Delta NO_y < -0.5$ ppb). The hourly average results for each scenario depicted by the solid and dashed lines were computed over all case study days.

production occurs during the afternoon period. The interesting result in Figure 7a is an average decrease of 20–25% in O$_3$ production rates from the base to the NO$_x$ reduction scenario during the afternoon hours. In fact, individual ΔC_{chem} values were consistently lower from the M02E04 scenario than results from the M02E02 base scenario on each day.

[22] Figure 7b displays the temporal behavior of ΔC_{vdif} and ΔC_{ddep} for layer 1. These two physical processes exhibit large magnitudes of nearly equal absolute value, however, they tend to cancel out each other since they are of opposite sign. Dry deposition is certainly a large loss term during most of the daytime period due to O$_3$ removal into the various surface vegetative types in the region. The downward vertical mixing rate term, acting to restore O$_3$ into layer 1, entrains higher O$_3$ values from adjacent vertical layers aloft and provides a strong positive contribution. Differences in the magnitudes of these physical processes between the modeling scenarios are rather small when averaged over the plume-print areas. However, it is apparent from Figure 7b that the differences gradually increased during the afternoon period with the NO$_x$ reduction scenario results being about 5% smaller than base case absolute values.

[23] The horizontal and vertical advection processes, which are strongly dependent on spatial O$_3$ concentration gradients, differed greatly and exhibited sign changes within the plume-impacted areas. Consequently, it was not meaningful to compute averages over spatial areas for these physical process terms in an effort to derive temporal variations. However, the magnitudes of the advection processes will be shown from a selected set of grid locations in a later section. Finally, results of analysis of the horizontal diffusion (ΔC_{hdif}) and cloud process (ΔC_{clds}) rate terms revealed both of these processes made negligible contribu-

tions to O$_3$ concentrations during these case study days and, hence, they are not discussed here.

3.3. Effects on O$_3$ Production Rates and Chemical Regime within Plume-Print Zones

[24] A more detailed investigation was undertaken to assess the impacts on the magnitudes of maximum O$_3$ production rates between these modeling scenarios in the vicinity of the major point sources owing to the notable spatial variability revealed earlier. This analysis also focused on results in the plume-print areas utilizing the ΔNO_y difference signatures in order to identify the highest ΔC_{chem} during afternoon hours on each case study day. Figure 8 displays the maximum O$_3$ production rates found in individual plume-print areas from the M02E02 scenario and the corresponding values in the same grid cell from the M02E04 scenario plotted against the O$_3$/NO$_x$ indicator ratio for all case study days. A large cluster of maximum ΔC_{chem} with many values in the range from 10 to 30 ppb/h occurs for the M02E02 scenario results at O$_3$/NO$_x$ ratios between 15 and 25. The broad variation in maximum ΔC_{chem} values is indicative of a large range in NO$_x$ emission rates among the point sources in the base case. Clearly, these high values reveal that rapid chemical O$_3$ production is indeed occurring downwind of many major point sources. These maximum chemical production rates were generally found from 2 to 5 grid cells (i.e., 24–60 km) downwind of point source grid locations. In contrast, relatively few maximum ΔC_{chem} values from the M02E04 scenario appear at O$_3$/NO$_x$ ratios <15, which defines the high NO$_x$, radical-limited regime [*Arnold et al.*, 2003] where O$_3$ is destroyed rather than produced when NO$_x$ concentrations are high. In addition, relatively few base case maximum ΔC_{chem} values are found at O$_3$/NO$_x$ ratios above 46, which denotes the NO$_x$-limited, photochemically aged region where very
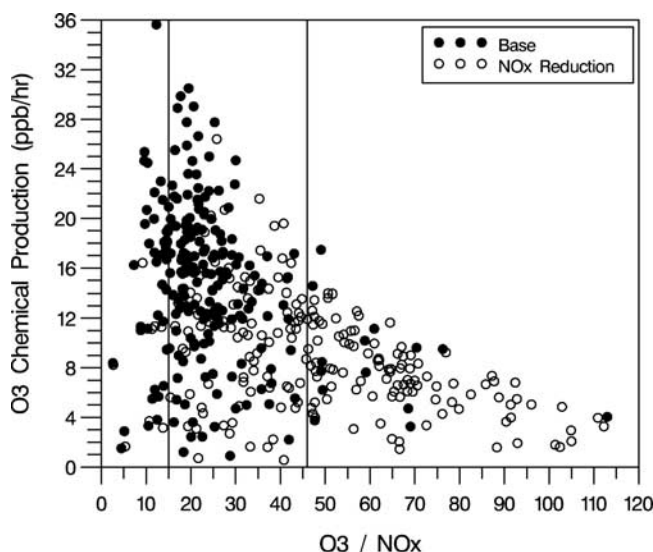
Figure 8. Maximum O$_3$ chemical production rates (ΔC_{chem}) found downwind of major point sources in the M02E02 results (solid circles) and the corresponding NOx reduction (M02E04) scenario results (open circles) during early afternoon hours (1700–1800 UTC) from all case study days are displayed versus O$_3$/NO$_x$ ratio. Ratio values of <15 and >46 denote NO$_x$-saturated and NO$_x$-sensitive regimes, respectively, while a chemically active transition zone exists between these limits.

low NO$_x$ concentrations exist [*Arnold et al.*, 2003]. In contrast, the ΔC_{chem} values from the M02E04 scenario are dramatically smaller and clustered at ratios closer to 46, and numerous values are even found at O$_3$/NO$_x$ ratios above 46. Thus, the results in Figure 8 suggest that these significant reductions in NO$_x$ emissions have caused a

distinct shift in the chemical state toward more NO$_x$-limited conditions downwind of many large point sources.

[25] These large decreases in maximum O$_3$ chemical production rates were in response to the significant NO$_x$ emission reductions. Consequently, a decline in surface NO$_x$ concentrations should also be discernable. It is of interest to identify evidence of a change in NO$_x$ concentrations that might be attributable to these point source emission reductions. The large decreases in modeled NO$_x$ concentrations aloft within the ORV region and downwind of it at a midmorning hour were comparable to the percentage reductions in NO$_x$ emissions [*Godowitch et al.*, 2008]. Although most surface NO$_x$ observation sites in the eastern U.S. are situated in urban and suburban locations making them strongly impacted by mobile NO$_x$ emissions and change in the mobile source sector, a strategically located rural NO$_x$ measurement site (AIRS ID 421255001) exists in southwestern Pennsylvania near the border with the West Virginia panhandle. It is in an ideally situated position downwind of the ORV source region during southwesterly wind flows for an examination of potential change in NO$_x$ that could be attributable to point source emission reductions.

[26] Results in Figure 9 display hourly averaged model and observed NO$_x$ concentrations from summer 2002 and 2004 days with southwesterly wind flows at this location. Our main interest herein is to ascertain a change in NO$_x$ rather than in a comparison of modeled and observed absolute concentrations. The M02E04 scenario results in Figure 9a illustrate an interesting feature, namely, a distinctive decline in NO$_x$ concentrations relative to the M02E02 scenario results beginning near 13 UTC (09 local time) and extending into the afternoon period. In fact, the NO$_x$ concentrations from M02E04 overlap the M04E04 results during most of the daytime period. Observed values in Figure 9b differ somewhat from the modeled results in the timing and magnitude of the early morning peak concen-
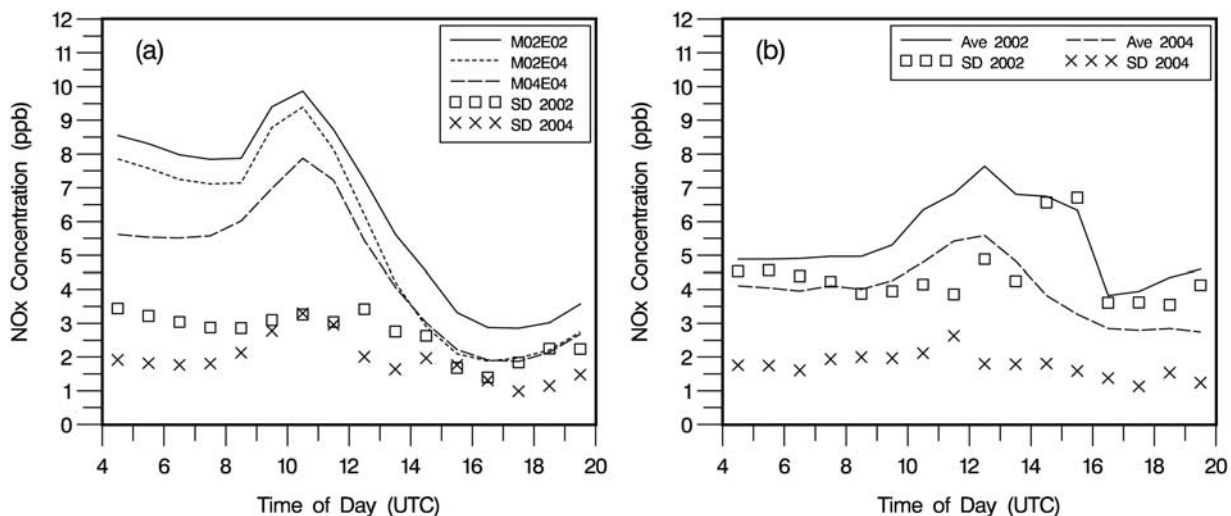

Figure 9. Temporal variation in the near-surface NO$_x$ concentration from southwesterly flow cases during the summers of 2002 and 2004 (a) for the modeling scenario results in the grid cell of the observation site and (b) at a rural southwestern Pennsylvania observation site in Washington, County (AIRS ID 421255001). The standard deviation (SD) for each hourly average is displayed. Local time is −4 h relative to UTC.
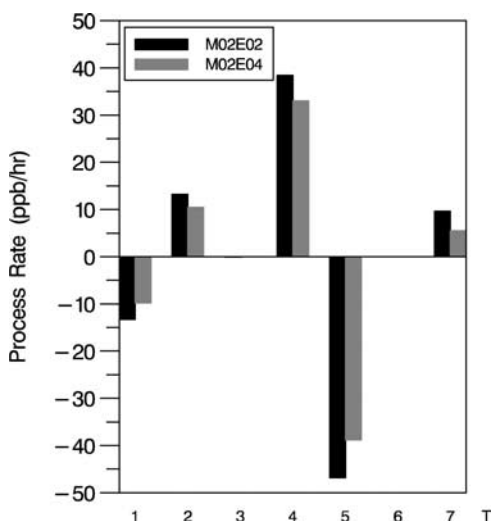
Figure 10. Integrated process rate terms from the M02E02 and M02E04 scenarios at the time (2000 UTC) of the maximum O$_3$ concentration on 11 August 2002 downwind of isolated point sources exhibiting substantial NO$_x$ emission reductions. The individual process rates are denoted by: 1, ΔC_{hadv}; 2, ΔC_{vadv}; 3, ΔC_{hdif}; 4, ΔC_{vdif}; 5, ΔC_{ddep}; 6, ΔC_{clds}; 7, ΔC_{chem}.

tration. It is noteworthy that Figure 9b shows observed NO$_x$ concentrations remain elevated until noon. During the late morning hours, downward entrainment of high NO$_x$ concentrations associated with elevated point source plumes occurs as the mixing height grows to plume heights. The large standard deviations (SD), which are comparable to average observed values during the late morning hours in the summer 2002 cases, indicate considerable variability in the observations. This is believed to be attributable to occasions of strong downward mixing of relatively high NO$_x$ concentrations from aloft. It is notable that observed NO$_x$ concentrations and SD values decreased from 2002 to 2004. The decreases in NO$_x$ concentrations over the 3-h period of 14–16 UTC were determined to be 35% and 42% in the model and observations, respectively, at this location, and are comparable to the percentage decrease in modeled NO$_x$ aloft. The observed NO$_x$ results from summer 2005 cases with this flow pattern (not shown) were found to be very similar to summer 2004 results.

3.4. Effects on Process Rates at the Downwind Locations of Maximum O$_3$

[27] The PA terms from both modeling scenarios were also examined in the surface grid cell locations of the maximum O$_3$ concentration found downwind of point sources to demonstrate the impact from sources in Figure 1 exhibiting the largest percentage NO$_x$ emission reductions. A set of 7 isolated major point sources was selected because the afternoon maximum O$_3$ concentrations downwind and their plume-print areas were readily discerned. The results from a single case study day (11 August 2002) are presented since they are similar to those found in the other cases. NO$_x$ emission rates were from 23 to 110 tons/d among the point sources, while the emission reductions were 85–92% between the M02E02 and M02E04 scenarios. The maxi-

mum 1-h O$_3$ concentrations found downwind of these point sources in the M02E02 results ranged from 75 to 90 ppb on this day.

[28] Figure 10 displays the averaged individual physical and chemical process rates from the downwind grid locations and at the time of the maximum O$_3$ concentrations for both modeling scenarios. The results show the contributions from the horizontal and vertical advection processes tend to cancel each other out. Likewise, although the absolute magnitudes of the vertical mixing and dry deposition processes rates are both large, they also nearly cancel out each other. Furthermore, results in Figure 10 reinforce those found earlier which reveal all process rates in the M02E04 scenario are reduced from M02E02 values. Values for ΔC_{hdif} and ΔC_{clds} are close to zero in this case. It is noteworthy that ΔC_{chem}, exhibiting a value near 10 ppb/h at this time and particular location, is about twice the M02E04 chemical production rate. Since the maximum O$_3$ concentration has been reached at this time, the net result from the sum of all process rates is close to zero.

[29] The key role that the chemical production rate plays in contributing to the increase in daytime O$_3$ concentrations that eventually led to afternoon values is further demonstrated in Figure 11. The evolution of the O$_3$ chemical production rate is shown in Figure 11a along with net values representing the sum of all physical process terms at the grid locations of the maximum concentrations downwind of these point sources. Results from the M02E02 scenario in a grid cell located outside the plume print of each point source are also displayed. Several interesting features are highlighted by the differences in the net physical and chemical process rates in Figure 11a. The averaged ΔC_{chem} values from the M02E02 scenario are greater than about 10 ppb/h for a 4–5 h span in the afternoon and are twice as large as the M02E04 scenario results. Furthermore, it is apparent that M02E04 chemical production rates have dropped to ΔC_{chem} levels found in the grid environment outside plume-print areas. A relevant aspect gained from the temporal evolution of the net of all physical terms is the important positive contribution to the O$_3$ concentration during the midmorning period, which is primarily due to the vertical mixing term as entrainment of higher O$_3$ aloft occurs into the growing mixing layer. During the morning period, the physical processes provide a comparable contribution to the increase in O$_3$ from chemical production which supports the results by *Zhang and Rao* [1999]. Nevertheless, sum of all physical process terms also represents a net loss for O$_3$ during the afternoon period and is counterbalanced only by the positive contribution from ΔC_{chem}. Consequently, the O$_3$ concentrations in Figure 11b increased as long as the chemical production rate exceeded the net loss of O$_3$ from the physical processes terms with deposition being the largest sink process at this grid position. Figure 11b shows that, although O$_3$ concentration differences between these scenarios are relatively small during the morning period, it is apparent that the greater chemical production exhibited in the M02E02 scenario results is the major factor contributing to the net increase in O$_3$ concentrations over an extended period of the afternoon. After the rapid rise during morning period, the O$_3$ concentration increase is much slower in the M02E04 scenario during the afternoon period and is comparable to
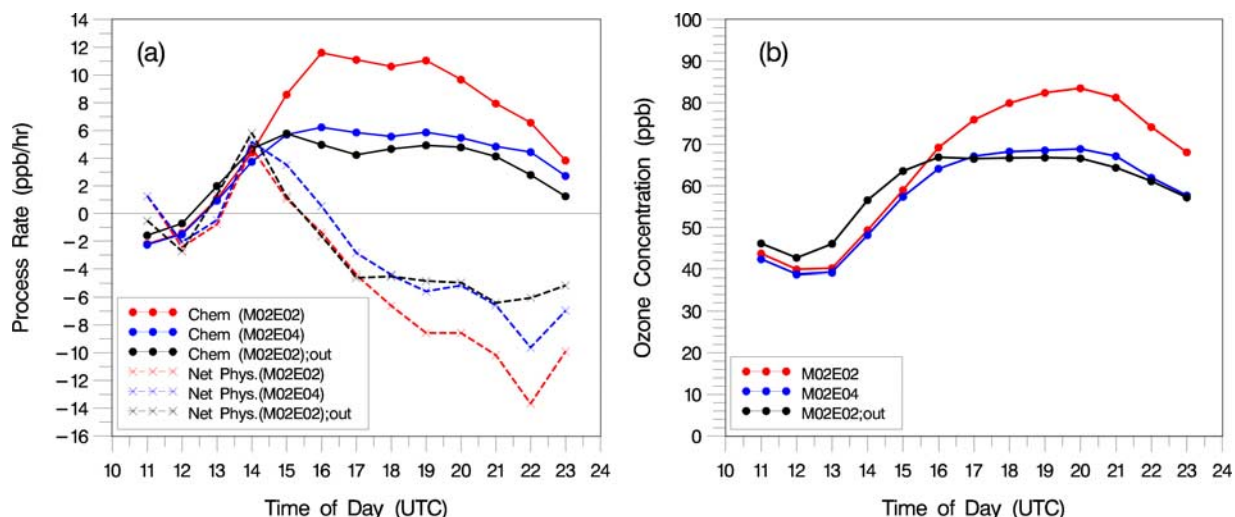
Figure 11. (a) Time variation of O$_3$ production rates (ΔC_{chem}) and net result of the sum of all physical process rates at the downwind grid location of the maximum O$_3$ concentration from selected major point sources for the base (M02E02) and emission reduction (M02E04) scenarios, and at selected grid cells outside the plume-impacted zone from the M02E02 scenario. (b) Evolution in O$_3$ concentration averaged from values at the downwind grid locations of the maximum ozone.

the concentration found outside the plume-impacted zones. In this case, the averaged maximum O$_3$ concentration downwind of this set of point sources dropped nearly 18% from 84 ppb to 69 ppb between the M02E02 and M02E04 scenarios.

[30] Results along trajectory paths were also explored to further investigate differences in the chemical production and concentrations downwind of major point sources at the surface and aloft from these modeling scenarios. The Hybrid Single Particle Lagrangian Integrated Trajectory (HYSPLIT) model [*Draxler and Hess*, 1997] was applied to generate trajectory paths starting at selected point source locations with the same meteorological fields used in the

CMAQ simulations. Ozone chemical production rates and concentrations were extracted from the 3-D output files in the grid cells along the trajectory path. The results along a particular trajectory spanning a 10 h period and traveling nearly 100 km downwind are displayed in Figure 12a. This trajectory was initiated at a late morning hour from the emission height of a major point emission source (i.e., Cumberland power plant plume) and ended before sunset. Although initially a negative ΔC_{chem} value exists aloft in the elevated source cell, there is considerable O$_3$ production in the M02E02 scenario aloft and at the surface (i.e., layer 1) for about 4 h of travel downwind. The O$_3$ chemical production rates traveling with the plume are much lower
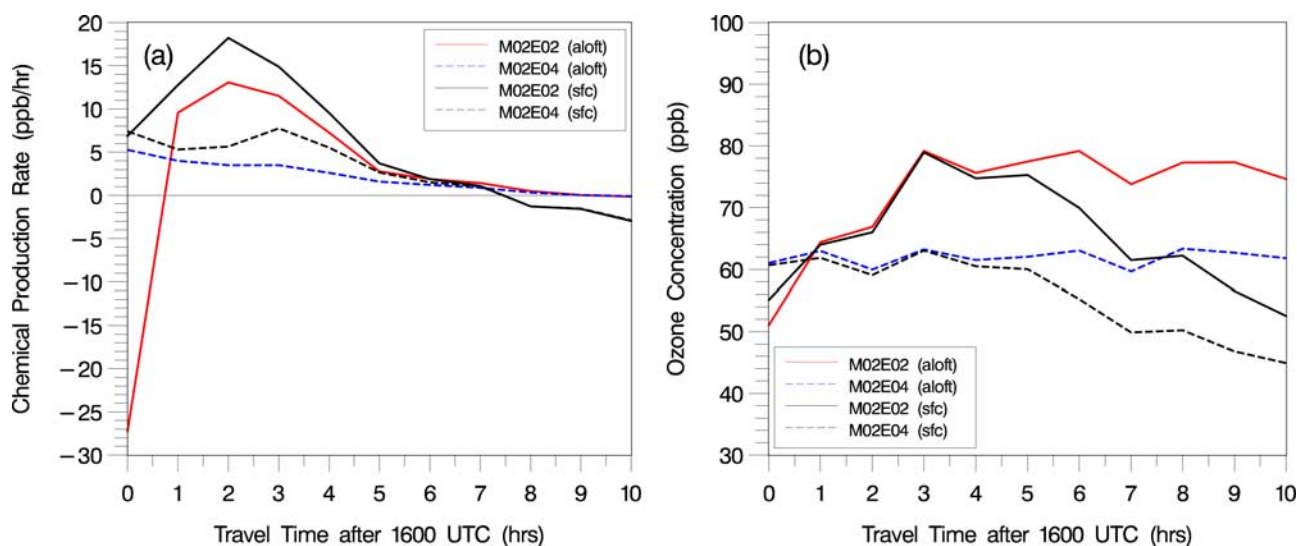

Figure 12. Evolution along a forward trajectory starting at 1600 UTC (1100 local time) from the emission height of a major elevated point source (600m AGL) in the (a) O$_3$ chemical production rate (ΔC_{chem}) and (b) O$_3$ concentrations from the M02E02 and M02E04 scenario results at the trajectory level and at the surface (layer 1).
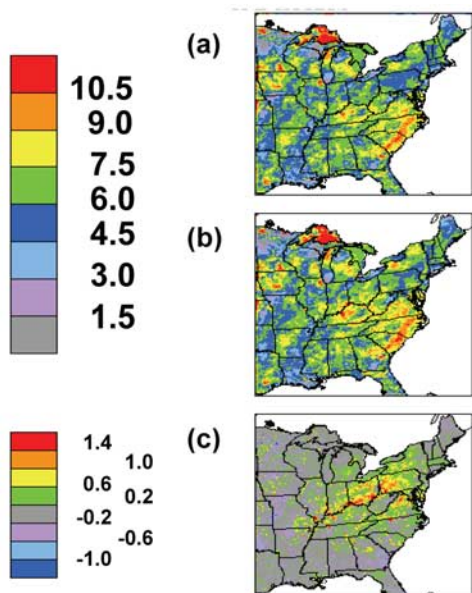
Figure 13. Spatial fields of the derived slope of the relationship between O$_3$ and NO$_z$ for the (a) M02E02 and (b) M02E04 scenarios, and (c) the difference in the slope between Figures 13b and 13a (e.g., M02E04 − M02E02).

in the M02E04 scenario with values closer to 5 ppb/h, which is attributed to relatively low NO$_x$ concentrations following an emission reduction of 90% at this source. While O$_3$ concentrations increased rapidly in the M02E02 results in Figure 12b, relatively little excess O$_3$ above background was generated following the plume in the M02E04 scenario.

[31] Figure 12b illustrates the differences in O$_3$ concentrations aloft and at the surface along the trajectory path between these model scenarios. Surface O$_3$ concentrations commence a distinctive decrease starting in the late afternoon (i.e., after 5 h travel time), while O$_3$ concentrations aloft exhibit relatively little temporal variation. A noteworthy result in this case is that O$_3$ aloft has been reduced by an average of about 18 ppb ($\approx$−22%) from nearly 80 ppb in the M02E02 scenario to 62 ppb in the M02E04 scenario downwind of these sources. Hence, a key outcome of the NO$_x$ emission reduction results is that lower O$_3$ concentrations are found both aloft and at the surface downwind of the major point sources at the end of a daytime period. In addition, declines in surface O$_3$ concentrations much further downwind are also anticipated when these reduced concentrations aloft are eventually mixed to the surface after transport during the nocturnal period.

3.5. Change in Ozone Production Efficiency Across the Region

[32] The relationship between O$_3$ and NO$_z$ (NO$_z$ = NO$_y$ − NO$_x$) concentrations has been used to quantify the impact of NO$_x$ emissions on ozone production. In particular, the slope of a linear regression between ozone and NO$_z$ is often termed the ozone production efficiency (OPE) and has been interpreted as the number of ozone molecules produced per molecule of NO$_x$ emitted before being oxidized [*Trainer et al.*, 1993; *Olszyna et al.*, 1994]. The analysis approach

adopted herein is the same as applied by *Olszyna et al.* [1994], which involved sorting ozone and NO$_z$ into 20 bins according to the level of NO$_z$ such that each bin contains 5% of all data points and then calculating the OPE as the slope of the linear regression through the bin averages. The hours considered in this analysis are restricted to the time period from 1000 to 1700 local time since values from these daytime hours can generally be characterized as representative of photochemically aged air in which ozone has been shown in the past to have had a linear relationship with NO$_z$ [*Trainer et al.*, 1993; *Olszyna et al.*, 1994].

[33] Resultant spatial fields of the slope of O$_3$/NO$_z$ shown in Figures 13a and 13b reveal broad areas of the domain with values ranging from about 5 – 8. The results in Figure 13c indicate an increase in OPE between the base and NO$_x$ reduction scenarios due to a discernable rise of slope across the ORV region and in the vicinity of other major point sources which experienced substantial NO$_x$ emission reductions. An increase in the slope of O$_3$/NO$_z$ relationship for the NO$_x$ reduction results is attributed to a greater decrease in the nitrogen product species contained in NO$_z$ compared to a relatively smaller change in O$_3$ concentrations. This finding provides additional evidence that the effect of the emission reductions in the ORV and at other point sources has transformed the ozone sensitivity closer to the surrounding environment that is primarily NO$_x$-limited.

[34] A comparison of modeled base case results with available measurements at various monitoring sites derived with the same method was also undertaken because capturing this relationship is crucial for the model to correctly quantify the impact of emissions changes. A scatterplot of modeled and observed O$_3$ and NO$_z$ concentrations shown in Figure 14 at a rural location (i.e., Pinnacle State Park) (J. J. Schwab et al., Ozone, trace gas, and particulate matter measurements at a rural site in southwestern New York State: 1995–2005, submitted to *Journal of the Air Waste Management Association*, 2008) in south-central New York state reveals greater variability in the observations than in
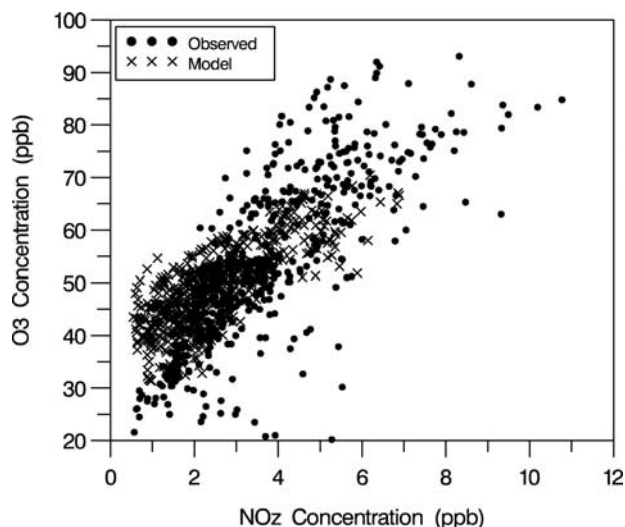

Figure 14. An example comparison of O$_3$ as a function of NO$_z$ from M02E02 results (crosses) and observations (circles) at a remote measurement site in Pinnacle State Park, New York, during the summer 2002 period.

Table 1. Observed and Modeled Results for the Slope of O$_3$ to NO$_z$ at Different Monitoring Sites

Site[a]	Observations	CMAQ-CB4
Pinnacle S.P., N. Y.	7.0	4.6
Harvard Forest, Mass.	9.9	5.1
SEARCH–Centreville	10.6	7.4
SEARCH–Jefferson St., Atlanta	4.9	6.6
SEARCH–Oak Grove	23.9	9.0
SEARCH–North Pensacola (OLF)	9.5	7.3
SEARCH–Pensacola	16.3	8.1
SEARCH–Yorkville	6.3	6.4
Illinois Beach S.P., Ill.	8.6	5.2
Winston-Salem, N. C.	6.1	6.1
Corbin, Va.	5.6	5.7

[a]S.P. denotes State Park. SEARCH denotes SouthEastern Aerosol Research and Characterization (SEARCH) study sites (www.atmospheric-research.com).

the model results. More importantly, a smaller slope is apparent in these model results with the CB4 chemistry. Results of the O$_3$/NO$_z$ slope at the Pinnacle site, as well as from other urban and rural measurement sites are listed against model values in Table 1. The modeled slopes (OPEs) are often lower than those derived at the different rural observation sites. *Yu et al.* [2006] also reported a lower OPE and a comparable difference as given in the Table 1 results for the Harvard Forest site from modeled results with the air quality forecast version of CMAQ during an episodic period in summer 2002. Future work is encouraged to focus on evaluating the chemical mechanisms used in regional air quality models.

3.6. Changes in the Spatial Ozone Correlation and Ozone Scales

[35] The spatial correlation structures were explored to study the interaction of synoptic-scale meteorological conditions that govern the transport of air masses, including ozone and its precursors across the region, with the spatial patterns and relative abundance of ground-level versus elevated emissions. The spatial correlation structures are estimated by determining correlation coefficients between spectrally decomposed time series of hourly O$_3$ at grid locations separated in space by a certain distance. In this analysis, the synoptic-scale component was estimated from the hourly modeled time series over the entire simulation period through the use of the Kolmogorov-Zurbenko (KZ) moving average filter as described by, among others, *Rao et al.* [1997] and *Hogrefe et al.* [2000]. Specifically, a centered moving average filter with a window length of 103 h was applied iteratively five times to determine the embedded synoptic forcing as the difference between the original time series and the filtered time series. The correlation patterns of the synoptic component provide a measure of the spatial coherency among ozone fluctuations at different locations and can be used to study communalities and differences between such fluctuations.

[36] Figure 15 shows an example of this method to determine the correlation coefficients between weather-induced variations in O$_3$ at a given reference location and other locations. In this analysis, the grid cell corresponding to the location of an ozone monitor in Columbus, OH was chosen as the reference location, and the colors plotted at

the location of all other grid cells indicate the strength of the correlation between the synoptic components in O$_3$ at that grid cell and the one at the reference location. The maps depict the results from six different model scenarios. Several features are evident from the results depicted in Figure 15. First, the correlation patterns in all of these scenarios represent a large spatial "footprint," with highest correlations at shorter distances and decreasing correlations at larger distances from the reference location. Second, some of these footprints are more elongated on a major axis along where correlations decrease more slowly than in the direction of the minor axis perpendicular to it. This feature is thought to be indicative of prevailing wind and transport patterns [*Rao et al.*, 1997]. Third, differences from the scenarios with 2002 versus 2004 emissions appear to be subtle for both the 2002 and 2004 meteorology. On the other hand, changing emissions to either the "no anthropogenic" or the "no controls" scenario, or utilizing 2002 versus 2004 meteorological conditions causes larger changes in the correlation patterns.

[37] To further study the relative impacts of these factors (i.e., emissions and meteorology) for a large number of reference locations, a quantity is defined to describe one of the distinctive features of each footprint. This quantity is the distance at which correlations between the reference location and the remote location drops below 0.37, referred to as the e-folding distance [*Rao et al.*, 1997]. This choice was made because a plot of correlations versus distance (group-
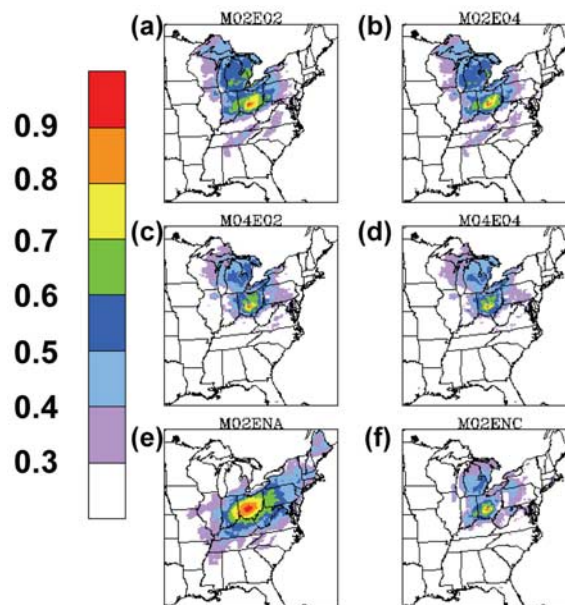

Figure 15. Correlation coefficient between synoptic-scale time series for the grid cell of a Columbus, Ohio, site and other grid cells for six different modeling scenarios. (a) Base 2002 (M02E02) and (b) NO$_x$ reduction scenarios (M02E04) with 2002 meteorology; (c) 2004 meteorology with 2002 emissions (M04E02) and (d) 2004 emissions (M04E04); and (e) no anthropogenic emissions using 2002 meteorology (M02ENA) and (f) no emissions control scenario with 2002 meteorology (M02ENC). Note that correlation values <0.3 are not displayed.
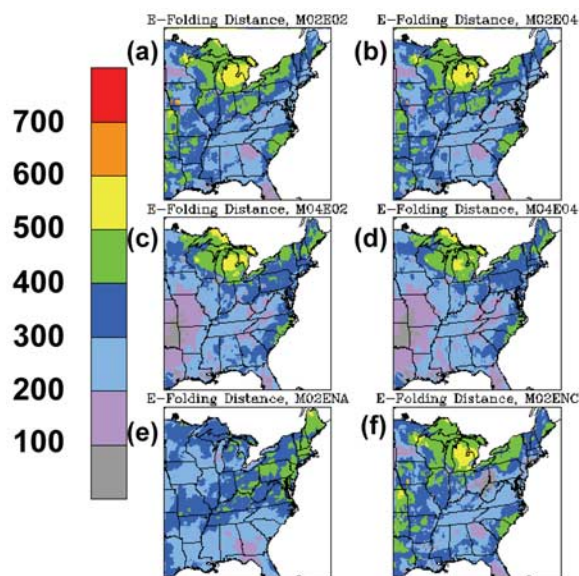
Figure 16. Spatial patterns of e-folding distances (kilometers) derived from six different modeling scenarios as in Figure 15.

ing correlations into different distance bins and then determining the average for each distance bin) generally follows an exponential decline. It should also be noted that such plots can be constructed for various quadrants to allow for the effects of prevailing winds. However, this approach decreases the sample size available for constructing averages in each distance bin. Since separate analyses (not shown here) found little qualitative benefit of performing this analysis isotropically versus anisotropically on the results to be shown, the e-folding distances were determined without grouping station pairs by direction.

[38] To investigate the effects of meteorology and emissions changes on these spatial correlation structures, maps of the e-folding distances for six CMAQ scenarios are displayed in Figure 16. In these maps, each grid cell is consecutively used as the reference point and the e-folding distance for the footprint using this grid cell as reference point is then calculated. The grid point is then colored to indicate the calculated e-folding distance and the procedure is repeated for all grid points. Results show that the e-folding distances are generally greater across the north central and northeastern areas of the modeling domain compared to the southeastern region. This may be partially attributed to more active weather patterns in the northern portion that transport ozone and its precursors over larger distances, compared to more frequent conditions with slower winds or more stagnation conditions in the southeastern U.S. [*Rao et al.*, 1997]. In addition, Figure 16 shows that for all scenarios, except the one without anthropogenic emissions (M02ENA), the e-folding distances are quite short in urban areas such as Chicago, Columbus, Pittsburgh, and New York City. This result is presumably due to titration of O$_3$ by fresh NO emissions that reduce correlations of ozone time series simulated in these locales compared with those simulated in more rural areas.

[39] Differences in the e-folding distances between pairs of scenarios, particularly against the 2002 base scenario (M02E02), are displayed in Figure 17. First, differences caused by changing the meteorology from 2002 to 2004, by completely eliminating anthropogenic emissions, or by using "no control" point source emissions are generally larger than those caused by reducing the point source NO$_x$ emissions from 2002 to 2004 levels. The effect of reducing the point source NO$_x$ emissions generally is to decrease the e-folding distances in the northern portion of the modeling domain by relatively small amounts. Second, compared to the 2002 base emissions scenario, the e-folding distances for the no anthropogenic emissions scenario show large increases in a band reaching from St. Louis eastward to Virginia and then northeast along the urban corridor, coinciding with high densities of anthropogenic emissions in the base case simulation. On a more local standpoint, isolated increases are also seen for urban areas such as Atlanta, Chicago, Columbus, and Pittsburgh, presumably due to the absence of the titration effect. In contrast, the e-folding distances decrease in southern areas presumably dominated by biogenic emissions. A plausible explanation for this feature might be that anthropogenic emissions in this area actually act to create a more homogeneous regional background while their absence increases the importance of smaller-scale land-use and circulation features that lead to
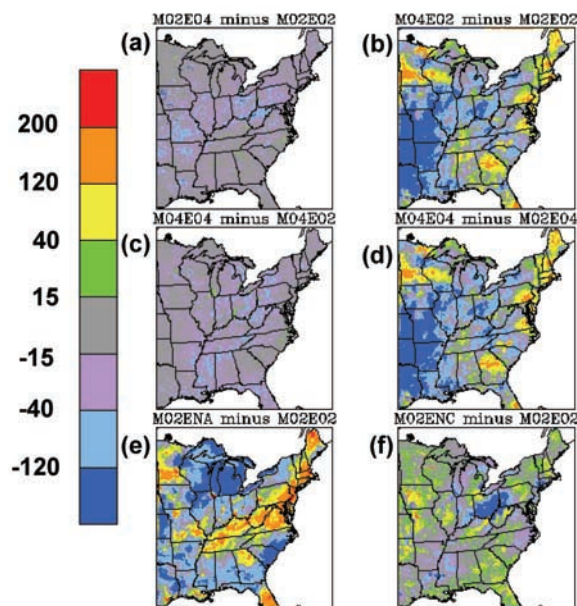

Figure 17. Maps of e-folding distance differences between pairs of modeling scenarios. (a) Effect of reducing point source NO$_x$ emissions using 2002 meteorology. (c) Effect of reducing point source NO$_x$ emissions using 2004 meteorology. (e) Effect of eliminating all anthropogenic emissions (biogenic emissions only) using 2002 meteorology. (b) Effect of 2002 versus 2004 meteorological differences using 2002 emissions. (d) Effect of 2002 versus 2004 meteorological differences using 2004 emissions. (f) Effect of no control CEMS emissions (1997 emission rates adjusted to 2002 heat input demand) versus 2002 emissions using 2002 meteorology.

shorter correlation distances. Support for this hypothesis comes from the panel showing changes in e-folding distances between the "no-control" case and 2002 base conditions. The larger NO$_x$ emissions in the M02ENC scenario generally lead to larger e-folding distances. Exceptions occur for the Ohio River Valley, Ohio, and the New Jersey/New York City/Connecticut metropolitan area where the large emissions increases in the "no control" scenario lead to much shorter e-folding distances. Ozone concentrations decreased in these areas in the "no-control" M02ENC scenario, supporting the notion that short e-folding distances are often indicative of areas in which locally high NO emissions quench ozone concentrations. It is evident that meteorological fluctuations as well as the spatial emission patterns and the relative contribution of low-level versus elevated emissions all influence the spatial coherency in weather-induced ozone fluctuations. Thus, this methodology has potential applications in the dynamic model evaluation approach [*Gilliland et al.*, 2008] where modeled and observation-based results are directly compared.

4. Summary

[40] Results from diagnostic methods here have examined the extent of change in the physical and chemical processes and chemical/transport indicators due to real-world point source NO$_x$ emissions reductions. Analyses focused on model results from a group of selected high-ozone days during summer 2002, which exhibited a high-pressure area within the eastern United States and southwesterly wind flows across the Midwest and Ohio River Valley. Similar analyses for other groups of summer cases under different synoptic-scale transport patterns would also be useful and in combination with these cases would to be representative of a summer season. Nevertheless, spatial patterns of process analysis results from our subset of days showed lower O$_3$ chemical production rates within plume-impacted areas in the NO$_x$ reduction scenario. Maximum rates of O$_3$ chemical production decreased by more than a factor of 2 downwind of major point sources experiencing the largest NO$_x$ emission reductions, which contributed to notable decreases in O$_3$ concentrations downwind at the surface and aloft. Additionally, large increases in the O$_3$/NO$_x$ ratio suggested a shift in the chemical regime toward more NO$_x$-limited conditions after the emission reductions. Evidence of decreases in surface NO$_x$ concentration due to the point source emission reductions in the ORV region was apparent, particularly during the midmorning and afternoon hours, in both observed and modeled results at a remote rural site in southwestern Pennsylvania. Correlation coefficients among weather-induced O$_3$ variations displayed smaller differences due to the emissions reduction compared to those obtained from hypothetical emission scenarios involving biogenic emissions only or from higher NO$_x$ emissions in a no control simulation. Relatively small differences in the e-folding distances were found between the base case and NO$_x$ emissions scenario results using the same meteorology. However, larger differences were uncovered when applying the same emissions with meteorology from different summer periods. Interestingly, a noticeable decrease in the e-folding distance was evident in the ORV source region under the no

control scenario, which is attributable to a decrease in ozone concentration from a sizable increase in NO$_x$ emissions. The results from this study should also be considered specific to this model configuration which involved CB4 chemistry, no subgrid plume treatment, and a 12-km grid cell resolution with 14 vertical layers.

References

Arnold, J. R., R. L. Dennis, and G. S. Tonnesen (2003), Diagnostic evaluation of numerical air quality models with specialized ambient observations: Testing the Community Multiscale Air Quality modeling system (CMAQ) at selected SOS 95 ground sites, *Atmos. Environ.*, 37, 1185–1198, doi:10.1016/S1352-2310(02)01008-7.

Byun, D. W., and J. Ching (1999), Science algorithms of the EPA Models-3 Community, Multiscale Modeling system, *EPA/600/R-99/030*, 611 pp., Environ. Prot. Agency, Washington, D. C. (Available at http://www.epa.gov/AMD/CMAQ/CMAQscienceDoc.html)

Byun, D., and K. L. Schere (2006), Review of the governing equations, computational algorithms, and other components of the Models-3 Community Multiscale Air Quality (CMAQ) modeling system, *Appl. Mech. Rev.*, 59, 51–77, doi:10.1115/1.2128636.

Draxler, R. R., and G. D. Hess (1997), Description of the HYSPLIT_4 modeling system, *NOAA Tech. Memo. ERL ARL-224*, NOAA, Silver Spring, Md. (Available at http://www.arl.noaa.gov/ready/hysplit4.html)

Environmental Protection Agency (2005), Evaluating ozone control programs in the eastern United States: Focus on the NO$_x$ budget trading program, *EPA454-K-05−001*, Environ. Prot. Agency, Washington, D. C. (Available at http://www.epa.gov/airtrends/2005/ozonenbp/)

Frost, G. J., et al. (2006), Effects of changing power plant NOx emissions on ozone in the eastern United States: Proof of concept, *J. Geophys. Res.*, 111, D12306, doi:10.1029/2005JD006354.

Gego, E., P. S. Porter, A. Gilliland, and S. T. Rao (2007), Observation-based assessment of the impact of nitrogen-oxide emissions reductions on ozone air quality over the eastern United States, *J. Appl. Meteorol. Climatol.*, 46, 994–1008, doi:10.1175/JAM2523.1.

Gego, E., P. S. Porter, A. Gilliland, C. Hogrefe, J. Godowitch, and S. T. Rao (2008), Modeling analyses of the effects of changes in nitrogen oxides emissions from the electric power sector on ozone levels in the eastern United States, *J. Air Waste Manage. Assoc.*, 58, 580–588.

Gilliland, A. B., C. Hogrefe, R. W. Pinder, J. M. Godowitch, K. L. Foley, and S. T. Rao (2008), Dynamic evaluation of regional air quality models: Assessing changes in O$_3$ stemming from changes in emissions and meteorology, *Atmos. Environ.*, 42, 5110–5123.

Gipson, G. L. (1999), Process analysis, in Science algorithms of the EPA Models-3 Community Multiscale Air Quality (CMAQ) modeling system, *EPA/600/R-99/030*, pp. 16.1–16.37, Environ. Prot. Agency, Washington, D. C.

Godowitch, J. M., A. B. Gilliland, R. R. Draxler, and S. T. Rao (2008), Modeling assessment of point source NO$_x$ emission reductions on ozone air quality in the eastern United States, *Atmos. Environ.*, 42, 87–100, doi:10.1016/j.atmosenv.2007.09.032.

Grell, G. A., J. Dudhia, and D. R. Stauffer (1994), A description of the fifth-generation Penn State/NCAR mesoscale model (MM5), *NCAR Tech. Note NCAR/TN-398+STR*, 138 pp., Boulder, Colo.

Hidy, G. M. (2000), Ozone process insights from field experiments Part I: Overview, *Atmos. Environ.*, 34, 2001–2022, doi:10.1016/S1352-2310(99)00456-2.

Hogrefe, C., S. T. Rao, I. G. Zurbenko, and P. S. Porter (2000), Interpreting the information in ozone observations and model predictions relevant to

regulatory policies in the eastern United States, *Bull. Am. Meteorol. Soc.*, *81*, 2083–2106, doi:10.1175/1520-0477(2000)081<2083:ITIIOO>2.3. CO;2.

Jang, J. C., H. E. Jeffries, D. Byun, and J. E. Plein (1995), Sensitivity of ozone to model grid resolution I. Application of high-resolution regional acid deposition model, *Atmos. Environ.*, *29*, 3085–3100, doi:10.1016/1352-2310(95)00118-I.

Jiang, G., B. Lamb, and H. Westberg (2003), Using back trajectories and process analysis to investigate photochemical ozone production in the Puget Sound region, *Atmos. Environ.*, *37*, 1489–1502, doi:10.1016/S1352-2310(02)01027-0.

Kim, S. W., A. Heckel, S. A. McKeen, G. J. Frost, E. Hsie, M. K. Trainer, A. Richter, J. P. Burrows, S. E. Peckham, and G. A. Grell (2006), Satellite-observed U. S. power plant, NO$_x$ emission reductions and their impact on air quality, *Geophys. Res. Lett.*, *33*, L22812, doi:10.1029/2006GL027749.

Olszyna, K. F., E. M. Bailey, R. Simonaitis, and J. F. Meagher (1994), O$_3$ and NO$_y$ relationships at a rural site, *J. Geophys. Res.*, *99*(D7), 14,557–14,563, doi:10.1029/94JD00739.

O'Neill, S. M., and B. K. Lamb (2005), Intercomparison of the Community Multiscale Air Quality Model and CALGRID using process analysis, *Environ. Sci. Technol.*, *39*, 5742–5753, doi:10.1021/es048403c.

Rao, S. T., I. G. Zurbenko, R. Neagu, P. S. Porter, J. Y. Ku, and R. F. Henry (1997), Space and time scales in ambient ozone data, *Bull. Am. Meteorol. Soc.*, *78*, 2153–2166, doi:10.1175/1520-0477(1997)078<2153:SATSIA>2.0.CO;2.

Sillman, S. (1999), The relation between ozone, NOx and hydrocarbons in urban and polluted rural environments, *Atmos. Environ.*, *33*, 1821–1845, doi:10.1016/S1352-2310(98)00345-8.

Trainer, M., et al. (1993), Correlation of ozone with NO$_y$ in photochemically aged air, *J. Geophys. Res.*, *98*(D2), 2917–2925, doi:10.1029/92JD01910.

White, A. B., L. S. Darby, C. J. Senff, C. W. King, R. M. Banta, J. Koermer, J. M. Wilczak, P. J. Neiman, W. M. Angevine, and R. Talbot (2007), Comparing the impact of meteorological variability on surface ozone during the NEAQS (2002) and ICARTT (2004) field campaigns, *J. Geophys. Res.*, *112*, D10S14, doi:10.1029/2006JD007590.

Xiu, A., and J. E. Pleim (2001), Development of a land surface model part 1: Applications in a mesoscale meteorology model, *J. Appl. Meteorol.*, *40*, 192–209, doi:10.1175/1520-0450(2001)040<0192:DOALSM>2.0.CO;2.

Yu, S., R. Mathur, D. Kang, K. Schere, B. Eder, and J. Pleim (2006), Performance and diagnostic evaluation of ozone predictions by the ETA-Community Multiscale Air Quality Forecast System during the 200 2 New England Air Quality Study, *J. Air Waste Manage. Assoc.*, *56*, 1459–1471.

Zhang, J., and S. T. Rao (1999), The role of vertical mixing in the temporal evolution of ground-level ozone concentrations, *J. Appl. Meteorol.*, *38*, 1674–1691, doi:10.1175/1520-0450(1999)038<1674:TROVMI>2.0.CO;2.

————————————

J. M. Godowitch and S. T. Rao, 109 T.W. Alexander Drive, U.S. Environmental Protection Agency (E243-01), Research Triangle Park, NC 27711, USA. (godowitch.james@epa.gov; Rao.ST@epa.gov)

C. Hogrefe, Atmospheric Sciences Research Center, University at Albany, State University of New York, Albany, NY 12222, USA. (chogrefe@dec.state.ny.us)